AGU PUBLICATIONS

JGR

Journal of Geophysical Research: Solid Earth

RESEARCH ARTICLE
10.1002/2017JB014730

Evaluating the Resolution of Deep Mantle Plumes in Teleseismic Traveltime Tomography

Ross Maguire[1], Jeroen Ritsema[1], Mickaël Bonnin[2], Peter E. van Keken[3], and Saskia Goes[4]

[1]Department of Earth and Environmental Sciences, University of Michigan, Ann Arbor, MI, USA, [2]Laboratory of Planetology and Geodynamics, CNRS, University of Nantes, Nantes, France, [3]Department of Terrestrial Magnetism, Carnegie Institution for Science, Washington, DC, USA, [4]Department of Earth Science and Engineering, Imperial College London, London, United Kingdom

Key Points:
- Resolution of deep mantle plume tails is always limited in regional-scale *P* and *S* traveltime tomography
- Optimal resolution of the plume tail requires networks with a wide aperture and dense station spacing
- Additional imaging improvements are obtained using finite frequency theory and using *SKS* traveltimes

Supporting Information:
- Supporting Information S1
- Data Set S1
- Data Set S2

Correspondence to:
R. Maguire,
romaguir@umich.edu

Citation:
Maguire, R., Ritsema, J., Bonnin, M., van Keken, P. E., & Goes, S. (2018). Evaluating the resolution of deep mantle plumes in teleseismic traveltime tomography. *Journal of Geophysical Research: Solid Earth*, *123*, 384–400. https://doi.org/10.1002/2017JB014730

Received 17 JUL 2017
Accepted 18 NOV 2017
Accepted article online 23 NOV 2017
Published online 10 JAN 2018

Abstract The strongest evidence to support the classical plume hypothesis comes from seismic imaging of the mantle beneath hot spots. However, imaging results are often ambiguous and it is questionable whether narrow plume tails can be detected by present-day seismological techniques. Here we carry out synthetic tomography experiments based on spectral element method simulations of seismic waves with period $T > 10$ s propagating through geodynamically derived plume structures. We vary the source-receiver geometry in order to explore the conditions under which lower mantle plume tails may be detected seismically. We determine that wide-aperture (4,000–6,000 km) networks with dense station coverage (<100–200 km station spacing) are necessary to image narrow (<500 km wide) thermal plume tails. We find that if uncertainties on traveltime measurements exceed delay times imparted by plume tails (typically <1 s), the plume tails are concealed in seismic images. Vertically propagating *SKS* waves enhance plume tail recovery but lack vertical resolution in regions that are not independently constrained by direct *S* paths. We demonstrate how vertical smearing of an upper mantle low-velocity anomaly can appear as a plume originating in the deep mantle. Our results are useful for interpreting previous plume imaging experiments and guide the design of future experiments.

1. Introduction

Seismic imaging of the structure of mantle plumes and constraining the role of plumes in the dynamics of the Earth remain important research objectives. Estimates of plume heat flux inferred from hot spot swells indicate that plumes carry 5–10% of the Earth's 44 TW (terrawatts) of heat (e.g., Sleep, 1990). Plumes may be responsible for the emplacement of large igneous provinces, continental breakup, and midplate volcanism (see Ballmer, van Keken, & Ito, 2015, for a review). Over the past two decades seismologists have sought evidence for plumes from estimates of the thermal perturbations of phase boundaries in the transition zone (e.g., Li et al., 2000; Schmandt et al., 2012; Shen et al., 1998) and from tomographic imaging (e.g., Allen et al., 1999; French & Romanowicz, 2015; Montelli et al., 2004; Wolfe et al., 1997, 2009).

Seismic tomography in particular is a powerful technique to illuminate plumes in the deep mantle and their interactions with large-scale flow and physical boundaries in the mantle transition zone. However, interpreting seismic models remains difficult for several reasons. First, seismic station coverage at hot spots, particularly in oceanic regions, is limited, which inhibits sampling of deep mantle structure with direct *P* and *S* waves. Waves that propagate nearly vertically through the mantle, such as *SKS*, sample the deep structure beneath hot spots but have limited vertical resolution. In regions with low and nonuniform data coverage regularization of the inversion may distort seismic velocity anomalies. The artificial elongation of velocity anomalies along near-vertical teleseismic raypaths complicates estimates of the depth extent of plumes. Second, the delays of seismic waves after propagating through narrow plume conduits in the lower mantle may be immeasurably small (e.g., Hwang et al., 2011; Maguire et al., 2016; Rickers et al., 2012). Finite frequency theory (e.g., Hung et al., 2001; Nolet & Dahlen, 2000) accounts for the effects of wave diffraction (i.e., wavefront healing) on traveltime delays. However, it is unclear if in practical terms finite frequency tomography offers higher image resolution compared with ray theoretical tomography when measurement errors and the contributions of shallow structure to traveltime delays are relatively large (e.g., Trampert & Spetzler, 2006).

We evaluate how thermal plumes are imaged in teleseismic traveltime tomography using resolution tests that are commonly applied to assess the potential artifacts in tomographic images (e.g., Grand, 1987; Spakman et al., 1989; Styles et al., 2011). Our models of thermal plumes are based on geodynamic predictions of the temperature structure in the mantle beneath plumes and mineral physics-based estimates of seismic velocities. We calculate the travel time signature of a set of dynamic plume structures using 3-D waveform simulations following our previous work (Maguire et al., 2016). We invert these "synthetic" data using both ray theory and finite frequency theory following methods using regional-scale teleseismic traveltime tomography. Our approach is similar to that of Rickers et al. (2012) and Xue et al. (2015) with the important difference that our plume structures are based on dynamically consistent compressible flow models of mantle plumes that satisfy geodynamic constraints together with a consistent mapping of temperatures to seismic velocity using mineral physics constraints. While plumes in the real Earth may deviate substantially from our idealized models, it is useful to consider geophysically plausible plumes since the range of widths, excess temperatures, and velocity perturbations are consistent with our current understanding of mantle dynamics and mineral physics.

While it is widely accepted that many hot spots exhibit upper mantle seismic anomalies, the debate on the resolvability of lower mantle plume tails continues. Therefore, our tests are focused on the imaging of the plume tail in the lower mantle. We do not explore in detail the structure of the plume head in the upper mantle which may be complicated by shearing driven by plate motion and dynamic layering (e.g., Ballmer et al., 2013). It is our goal to explore how accurately narrow plume tails can be imaged with regional seismic networks, given limited data coverage, inversion regularization, and data uncertainty. In synthetic tomography experiments, we vary the source-receiver geometry to determine the effects of array aperture and station density on image resolution. We choose regional-scale deployments since the direct phases *S* and *P* are ideal phases to image the deep mantle especially when they are recorded by wide-aperture, dense regional networks. We estimate the additional resolving power of *SKS* waves and assess the value of finite frequency theory over ray theory. We use Hawaii as our example target and evaluate how well a plume there can be imaged using past and planned offshore seismic deployments in the Pacific Ocean.

2. Methods

2.1. Numerical Simulations of Plumes

2.1.1. Geodynamic Modeling

The tested plume structures are based on geodynamic simulations of flow in the Earth using the method previously described by Maguire et al. (2016) and Bossmann and van Keken (2013). We simulate plumes in a compressible mantle by solving the equations governing conservation of mass, momentum, and energy using the finite element method in an axisymmetric spherical shell. Plumes are initiated by applying a harmonic perturbation to the thermal boundary layer above the core-mantle boundary (CMB).

We focus on three plumes with different diameters and strengths (Figure 1). The range of dynamic parameters is summarized in Table 1. The buoyancy flux of the plume tails varies between 1.5 and 3.0 Mg/s, which is consistent with the range of hot spot buoyancy fluxes reported in Sleep (1990). The plume structure depends on several factors, including the temperature contrast across the core-mantle boundary ΔT_{CMB}, the depth dependence and temperature sensitivity of viscosity, the thermal expansivity and conductivity, and the Clapeyron slope Γ_{660} of the ringwoodite-bridgmanite transition near a depth of 660 km (abbreviated as the "660" from hereon). We use a temperature- and depth-dependent viscosity $\eta(T,z) = \eta_0(z)\exp(-b(T - T_{\mathrm{ref}}))$ which represents a linearization of the Arrhenius viscosity law. We choose b to be in the range of $\ln(10^1)$ to $\ln(10^3)$. The latter value is consistent with olivine under diffusion creep with an activation energy of $E = 300$ kJ mol^{-1}. The depth-dependent viscosity profile $\eta_0(z)$ is defined by three layers. In the lower mantle $\eta_0(z) = 10^{22}$ Pa s. In the upper mantle we reduce the viscosity by a factor of 30 in a number of models. The uppermost 120 km of the mantle represents a high-viscosity lithosphere with $\eta_0(z) = 10^{24}$ Pa s.

Models R1a, R1b, and R1c represent three stages of development of the same dynamic simulation. After 45 Myr, plume R1a is a starting plume with a head rising in the lower mantle. After 55 Myr, plume R1b has reached the upper mantle and has begun to spread beneath the lithosphere. The plume structure is complex near the 660 because this boundary partially impedes the flow. After 175 Myr, plume R1c has a quasi steady state structure. Phase boundary effects have dissipated and the plume head has spread completely beneath the lithosphere. Its tail in the lower mantle has a cylindrical structure with a width of about 500 km.

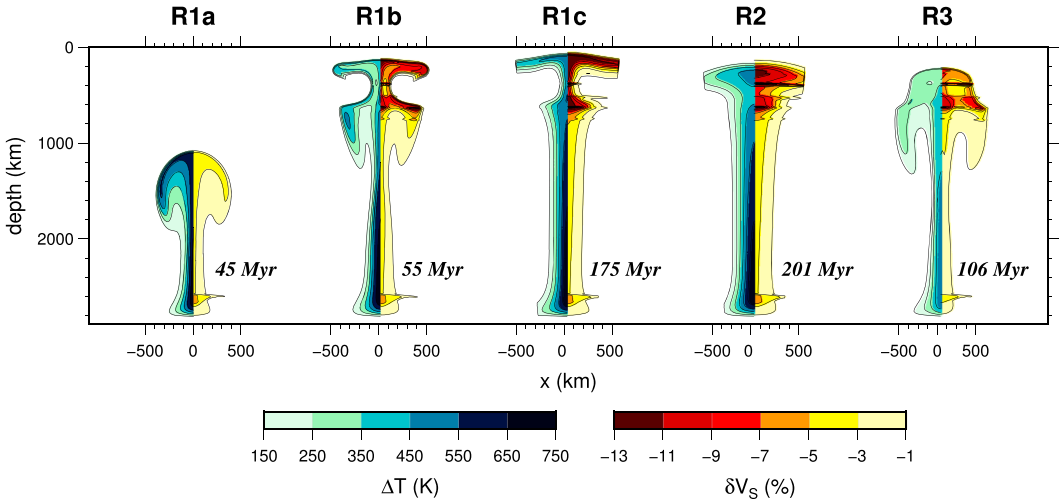

Figure 1. Dynamic simulations of plumes used in sensitivity tests. The plumes are symmetric about the vertical axis at $x = 0$. For each plume, the excess temperature is shown on the left and the reduction in shear velocity δV_S relative to PREM is shown on the right. The plume structures R1a, R1b, and R1c are snapshots of the same dynamic simulation at 45 Myr, 55 Myr, and 175 Myr, respectively.

R1c is thinner in the asthenosphere by a factor of about 2 due to the viscosity reduction above 660. Plume R2 has an anomalously wide (about 800 km) tail due to the modest temperature dependence of viscosity compared to the other models. Plume model R3, on the other hand, has an anomalously thin (less than 400 km wide) and weak tail because the temperature contrast across the CMB is relatively small at 550 K and the viscosity is strongly temperature dependent ($b = \ln(10^3)$). The heads of plumes R1c and R2 have spread horizontally a significant distance beneath the lithosphere. We artificially truncate them to be no wider than 5° from the plume axis, so they do not overwhelm the traveltime delay signal from the tail in the deep mantle.

We do not model any thermochemical plumes and therefore ignore the complexities that may arise when chemical entrainment of a dense layer is modeled. Lin and van Keken (2006) and Dannberg and Sobolev (2015) showed that entrainment of dense eclogitic material may reduce plume buoyancy and broaden plumes in the lower mantle. In addition, nonperidotitic components could change the amplitude of the seismic anomaly. While plumes R1, R2, and R3 are purely thermal in origin, the travel time delays in the plume tails are approximately linear with respect to velocity perturbation (e.g., Maguire et al., 2016; Mercerat & Nolet, 2013). Therefore, our results can provide insight into the resolvability of stronger or weaker thermochemical plume tails with similar widths.

2.1.2. Seismic Velocity Structure of Plumes

The calculation of the seismic velocity structure of plumes R1, R2, and R3 in Figure 1 follows the same steps as in Maguire et al. (2016). We assume a constant pyrolitic composition (Workman & Hart, 2005), defined in terms of the six oxides Na_2O, CaO, FeO, MgO, Al_2O_3, and SiO_2. Using the code Perple_X (Connolly, 2005) and the thermodynamic database of Stixrude and Lithgow-Bertelloni (2011), we compute the equilibrium mineral assemblage and the corresponding elastic parameters and density as a function of pressure and temperature. The seismic velocity of the bulk mineral assemblage is the Voigt-Reuss-Hill average of the velocity

Table 1
Dynamic Parameters Used in Plume Simulations

Plume	Ra	ΔT_{CMB} (K)	b	Γ_{660} (MPa K^{-1})
R1	2×10^6	750	$\ln(10^2)$	−2.5
R2	1×10^6	750	$\ln(10)$	0
R3	8×10^5	550	$\ln(10^3)$	−2.5

Note. Ra is the thermal Rayleigh number, ΔT_{CMB} is the temperature contrast across the core-mantle boundary, b is the temperature dependence of viscosity, and Γ_{660} is the Clapeyron slope of the wadsleyite-bridgmanite phase transition.

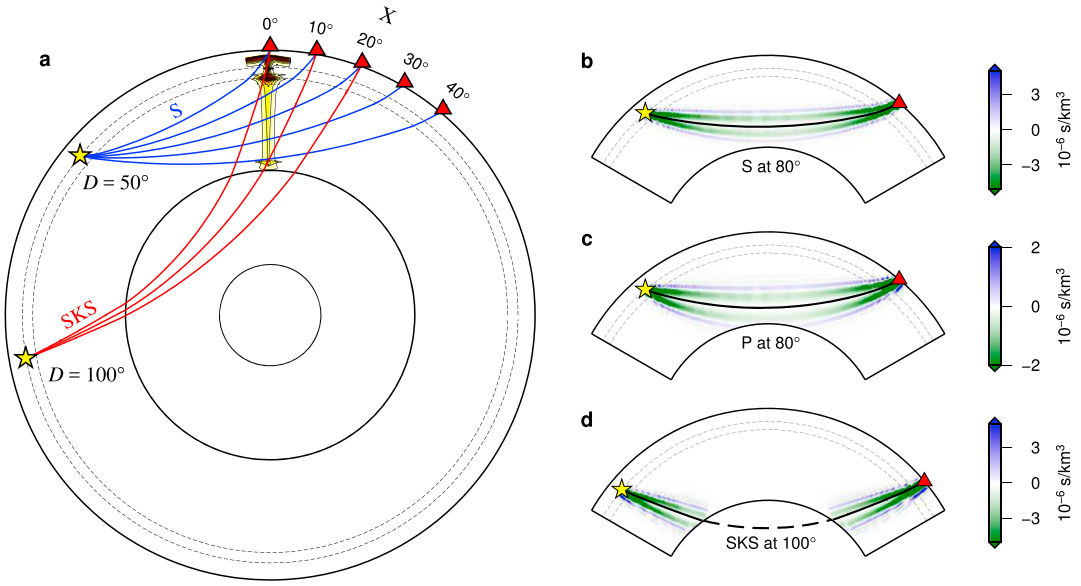

Figure 2. (a) Ray geometry for *S* (in blue) and *SKS* (in red) waves traversing plume R1c. The distance *D* between the earthquake and plume is 50° for *S* and 100° for *SKS*. *X* is the angular distance beyond the plume along the great circle path. (b–d) Sensitivity kernels $K(\mathbf{x})$ for cross correlation travel time delays measured over the frequency band 0.04–0.10 Hz. Kernels are shown for an *S* wave at an epicentral distance of 80° (in Figure 2b), a *P* wave at 80° (in Figure 2c), and an *SKS* wave at an epicentral distance of 100° (in Figure 2d). The yellow star indicates the earthquake and the red triangle indicates the receiver. Earthquakes are 400 km deep. The black lines in the center of the kernels are the geometric raypaths.

of each phase. Subsequently, we add the effects of temperature, pressure, and frequency-dependent anelasticity using model Q7g (as in Maguire et al., 2016). The maximum velocity reduction within plume tails is about 4% for shear waves and 2% for compressional waves. Cobden et al. (2008) provide further details of the thermodynamic method including sources of uncertainty.

2.2. Seismic Modeling

2.2.1. Computation of Travel Time Delays

The Preliminary Reference Earth Model (PREM) (Dziewonski & Anderson, 1981) is our reference seismic structure of the mantle without plumes. We construct seismic structures for plumes R1, R2, and R3 by superposing their velocity perturbations (from Figure 1) on PREM. We note that the choice of reference structure is not an important factor in our analysis given that commonly used 1-D Earth models deviate only slightly in the lower mantle. We determine the traveltime delays of the phases *P*, *S*, and *SKS* using spectral element method (SEM) waveform simulations. The seismic wavefield is described within each element as an expansion in fourth-order Lagrange polynomials. The SEM waveforms are accurate to wave periods longer than 10 s, corresponding to wavelengths in the lower mantle of 130 km (for *P* waves) and 80 km (for *S* waves). In contrast to our previous work (Maguire et al., 2016) which was based on SES3D (Gokhberg & Fichtner, 2016), we use the spectral element code SPECFEM3D GLOBE (Komatitsch & Tromp, 2002) to simulate the waveforms of core phases.

We analyze synthetic waveforms at teleseismic distances. As an example, Figure 2a shows the raypaths of *S* and *SKS* propagating through plume R1c for two events at distances $D = 50°$ (for *S*) and $D = 100°$ (for *SKS*) from the plume axis. When the plume axis is at a distance *D* of 50° from the event, the *S* waves at epicentral distances between 60° and 90° cross the plume tail in the lower mantle. The *SKS* waves traverse the plume tail more vertically up to an epicentral distance of 110° when the plume event distance *D* is 100°.

We calculate traveltime differences for *P*, *S*, and *SKS* between PREM and the 3-D plume structures by comparing waveform segments centered on *P*, *S*, and *SKS*. The windows are approximately 50 s wide. The seismograms are bandpass filtered between 0.1 Hz and 0.04 Hz. We consider cross correlation delay times when applying finite frequency tomography and onset delay times when applying ray theoretical tomography since the wave onset is a high-frequency signal of a waveform. We discard measurements for waveforms affected by the interference between *S* and *SKS* near an epicentral distance of 80°.

2.2.2. Tomographic Inversion

We invert travel time delays to estimate *P* wave and *S* wave structure using either ray theory (RT) or finite frequency theory (FF) following the procedures that have been applied to regional network data (e.g., Bonnin et al., 2014). The theories provide fundamentally different relationships between velocity heterogeneity in the mantle and recorded traveltime delays. According to RT, the travel time delay is sensitive to wave speed variation along the raypath *S*:

$$\delta T = -\int_S \frac{\delta v}{v^2}\,\mathrm{d}s, \tag{1}$$

where v is the absolute seismic velocity and δv is the fractional perturbation relative to v. In FF, the travel time delay is influenced by seismic structure within a volume V surrounding the raypath:

$$\delta T = \int_V K(\mathbf{x})\,\delta v\,\mathrm{d}V, \tag{2}$$

where the sensitivity kernel $K(\mathbf{x})$ is related to the Fresnel zone.

Figures 2b–2d illustrate the cross-sectional form of $K(\mathbf{x})$ for *S*, *P*, and *SKS* measurements, respectively. *S* and *P* kernels are shown for events recorded at an epicentral distance of 80° and the *SKS* kernel is shown for an event recorded at epicentral distance of 100°. The kernels reflect the sensitivity of cross correlation delay time observations to waves filtered between 10 s $< T <$ 25 s period. At the wave turning depth, the kernel is about 1,000 km wide but the width depends on epicentral distance and wave period. We compute the kernels $K(\mathbf{x})$ for PREM using the paraxial ray approximation introduced by Dahlen et al. (2000). We ignore the effects of velocity structure on the raypath *S* and on the sensitivity kernels $K(\mathbf{x})$ which we expect to be weak for plume tails (e.g., Mercerat & Nolet, 2013).

The model $\mathbf{m}$ is based on the cubed-Earth parameterization (e.g., Bonnin et al., 2014; Charléty et al., 2013) and consists of about 3.5×10^6 blocks with horizontal side lengths between 59 and 83 km and vertical side lengths between 44 and 90 km which increase with depth. The global parameterization accommodates both mantle and core phases at teleseismic distances. The size of each voxel is small compared to the width of the finite frequency sensitivity kernels. The distinct 3-D shapes of the kernels are preserved when projected onto the parameterization (Chevrot et al., 2012).

Given the large number of model parameters, we regularize the inversion by applying norm damping (i.e, the total size of the model) and smoothness damping (i.e., the second spatial derivative of the model). We minimize the object function $O(\mathbf{m})$

$$O(\mathbf{m}) = \chi^2 + \epsilon_n\,\mathbf{m}^2 + \epsilon_s\,(\mathbf{Sm})^2. \tag{3}$$

The first term of $O(\mathbf{m})$ represents the data misfit. The second and third terms represent the model size and the model roughness, respectively. The system matrix $\mathbf{G}$ incorporates the forward theory, $\mathbf{d}$ is the vector of travel time delays, ϵ_n and ϵ_s are the norm and smoothness damping parameters, and $\mathbf{S}$ is a smoothness matrix which minimizes the Laplacian of the model.

The data misfit, χ^2, is defined as

$$\chi^2 = \sum_i^N \frac{(\sum_j G_{ij} m_j - d_i)^2}{{\sigma_i}^2}, \tag{4}$$

where N is the number of data and i and j are the indices of traveltime delays and model parameters, respectively. When the model fits the data to within measurement uncertainties, $\chi^2 = N$. We add varying amounts of Gaussian noise to the synthetic delay time data to approximate random measurement error.

We experiment with different values of the measurement uncertainty σ to estimate preferred models $\mathbf{m}$. We choose the minimum value for σ of 0.1 s, which is equivalent to the time step in the waveform simulations. The maximum value of σ is 1.0 s or 10% of the dominant wave period. It represents a realistic error when the match between observed and synthetic waveforms is poor and when the effects on waveforms of the crust, anisotropy, and 3-D heterogeneity in the deep mantle are uncertain.

We determine the optimal model, by varying the values of ϵ_s and ϵ_n while setting their ratio constant ($r = \epsilon_s/\epsilon_n$). Our tests indicate that $r = 5$ provides a suitable balance between smoothness and norm damping,

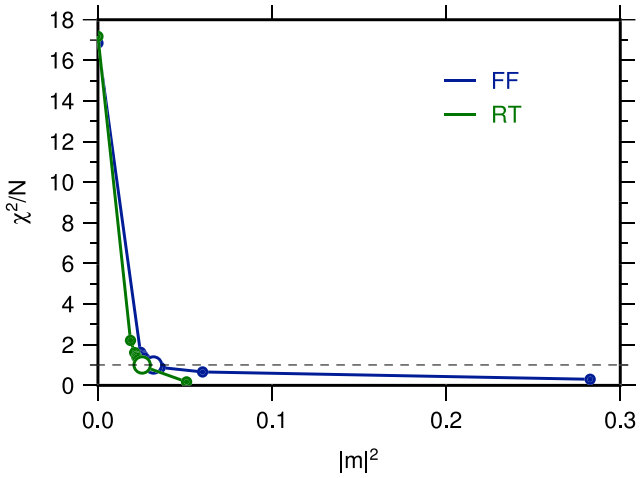

Figure 3. The tradeoff curve of misfit versus model norm obtained for plume R1a using network configuration A (see section 3.1). Results for FF are shown in blue and results of RT are shown in green. The open circles indicate the "best" model, for which the model fits the data to within uncertainty (i.e., $\chi^2 = N$). The best model **m** is smaller for RT than FF for a given misfit χ^2.

and we use this value for all inversions unless otherwise noted. The effect of the choice of regularization parameters is explored in section 4.7.

Figure 3 shows an example of tradeoff curves used to determine the best fit model for both RT and FF. In both RT and FF the optimal model is near the bend of the tradeoff curve, which indicates that error estimates are well constrained. However, for a given variance reduction χ^2/N, FF always leads to a model **m** with a larger L2 norm, indicating that FF recovers images of plume structures with higher amplitudes.

3. Network Configurations

Seismic network configuration and wave sampling are the key factors determining tomographic image resolution. To understand plume resolution given the practical limitations of network design, especially in ocean basins, we conduct tomographic inversions of the synthetic traveltime data for four different network configurations. We determine the resolution of plumes given (i) ideal data coverage and (ii) incomplete data coverage that is representative of past or newly designed experiments near Hawaii and in the Pacific Ocean.

3.1. Configuration A: Large Network Aperture, Small Station Spacing, and Homogeneous Event Distribution

An ideal seismic network has a wide aperture with dense station spacing and records earthquakes over a full range of epicentral distances and azimuths. Here we assume such a network to be a square grid of stations with a width L and station spacing Δx. The events are at distances D between 30° and 120° and at azimuths every 30° (Figure 4a).

We vary L and Δx to explore how network aperture and station density affect resolution. For the largest and densest grid, when L = 6,000 km and Δx = 100 km the data coverage is optimal, because the inversion results do not improve appreciably if the network aperture L is larger or if station spacing Δx is smaller. The largest network considered provides 254,193 paths for P and S.

3.2. Configuration B: the PLUME Geometry

The Plume-Lithosphere Undersea Melt Experiment (PLUME) (Laske et al., 2009; Wolfe et al., 2009) was a comprehensive seismic experiment aimed at imaging the mantle beneath the Hawaiian hot spot. The experiment consisted of 67 land and ocean-bottom seismometers on and surrounding Hawaii which were in operation for more than 2 years. Figure 4b shows the station distribution of the PLUME experiment, following the description of Wolfe et al. (2009). The network aperture is over 1,000 km, with stations typically spaced about 100 km apart. In simulating a set of traveltimes, we use earthquake locations from all events greater than M_w 6 that occurred during the 2 year deployment of the PLUME network at epicentral distances between 30° and 120°. The events are not exactly the same as those used by Wolfe et al. (2009), which were selected on the basis of waveform quality, but the azimuthal and distance distributions are similar. The total number of raypaths for P and S waves is 5,276.

3.3. Configuration C: Wide-Aperture Linear Arrays

The small array aperture of the PLUME experiment limits the imaging of lower mantle beneath Hawaii. Here we explore how tomographic resolution can be improved if a hypothetical seismic array deployment has a wider aperture and would be operating for a longer time. The deployment consists of three linear arrays which intersect at Hawaii (Figure 4c). The station spacing is Δx = 200 km, and the length of each array is 50°. The total number of seismometers is 87. In our test the angles between each limb of the array is 60° and is optimally aligned with regions of relative high seismicity. We consider a 5 year deployment and simulate traveltime measurements for all teleseismic earthquakes greater than M_w 6 that have occurred between 2012 and 2017, which provides 50,738 raypaths for P and S waves.

3.4. Configuration D: The Pacific Array

The fourth network configuration is based on a conceptual Pacific-wide network called "The Pacific Array" as envisioned by Kawakatsu et al. (2016). The anticipated configuration of the Pacific Array (PA) is shown in Figure 4d. The PA constitutes constitutes "an array of arrays." Each of the 14 subarrays is comprised of a spiral of 10 stations with an aperture of about 500 km which enables the measurement of surface wave dispersion

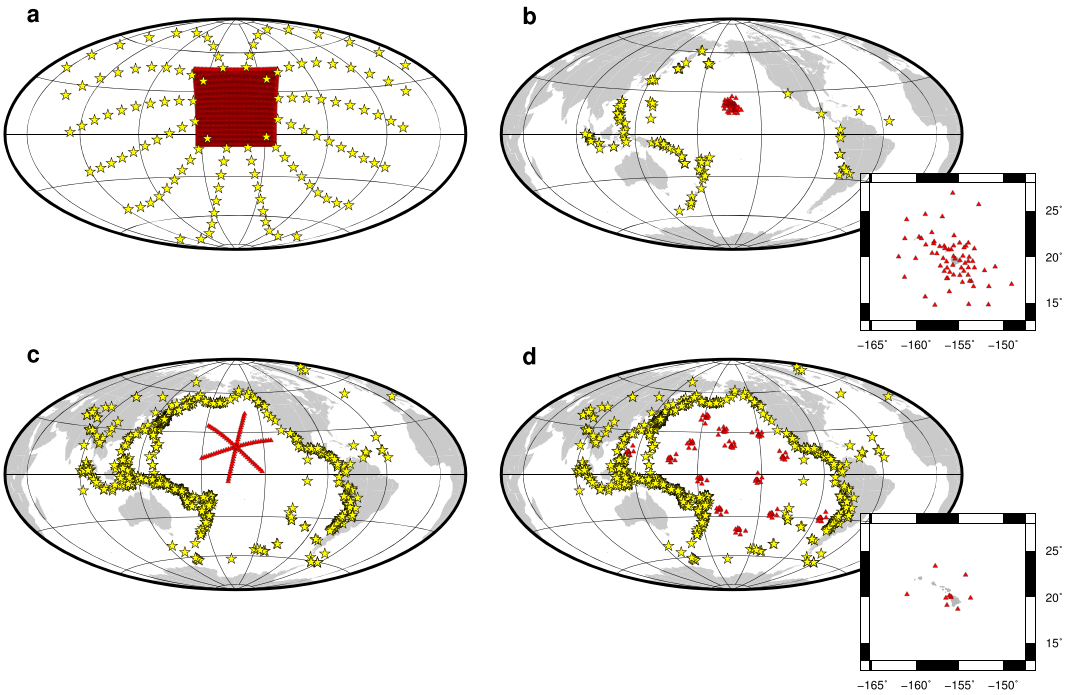

Figure 4. Source-receiver geometries used in synthetic tomography experiments. Yellow stars indicate earthquakes and red triangles indicate receivers. (a) A scenario in which earthquakes are recorded on a rectangular network at distances D between 30° and 120° and with uniform azimuthal coverage. The width L of the network is 6,000 km, and the spacing between stations Δx is 100 km. (b) The network geometry shown is identical to the PLUME geometry (Wolfe et al., 2009). The earthquakes are larger than magnitude 6 between 2012 and 2017. (c and d) Hypothetical deployments in the Pacific Ocean. The earthquake locations are taken from the historical seismicity record of events greater than M_w 6 over the previous five years. The network in Figure 4c comprises three intersecting linear arrays with $\Delta x = 200$ km. The arrays-of-arrays network shown in Figure 4d is similar to the proposed Pacific Array. The insets in Figures 4b and 4d show a closeup of the stations near Hawaii.

to study the structure of the crust and lithosphere across the Pacific. The network as a whole provides improved body wave coverage of the deep mantle. We assume in our modeling that the PA would have been active for the same 2012–2017 period as the previous configuration. The array provides 62,715 direct body wave paths over this time span.

4. Results

We first explore the impact of plume tail width on resolution by showing inversion results for each plume structure using the optimal source-receiver configuration. We next illustrate how data coverage and other aspects of the inversion process affect image resolution.

4.1. Plume Images for Ideal Data Coverage

Figure 5 shows the resolved images of plumes R1 (at stages a, b, and c), R2, and R3 using FF and RT inversions of S wave delay times. We use network configuration A shown in Figure 4a with $L = 6{,}000$ km and $\Delta x = 100$ km and assume that the uncertainty in the S wave traveltime delays has a Gaussian distribution with a standard deviation $\sigma = 0.1$ s. This represents an optimal scenario for a tomographic inversion of teleseismic traveltimes at a regional network of stations: the network aperture is wide, the station spacing is small, the earthquake distribution is uniform, and the traveltime measurements are precise.

Despite the optimal setup, the images derived using both RT and FF reveal the significant distortions and amplitude loss. The intricate head and stem features of the plume in the upper mantle (e.g., plumes R1b and R1c) or lower mantle (e.g., R1a), the dynamic effects of the 660 on plume ascent, and the thinning of the conduit in the low-viscosity upper mantle above the 660 are unresolved. The velocity anomaly of the plume in the lower mantle is strongly reduced due to wavefront healing and the applied model damping. For the same variance reduction, FF resolves the plume tail in the lower mantle with a higher amplitude than RT. For example, $\delta V_S = -1\%$ in the resolved plume tail of R1b imaged with FF, while is only about −0.2% with RT δV_S.

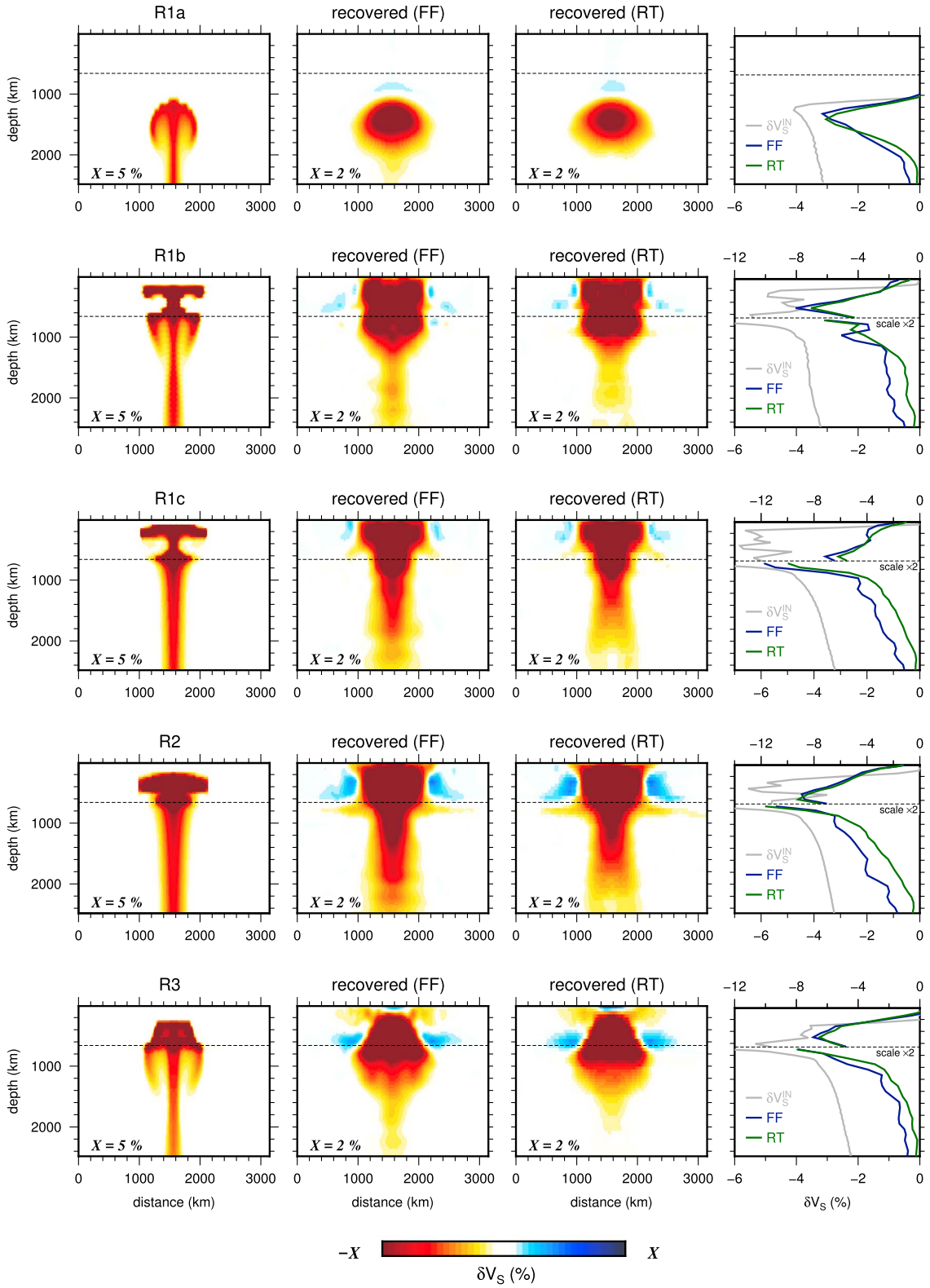

Figure 5. Shear velocity structures of the plumes R1, R2, and R3 obtained by inverting *S* wave delay times for network geometry A (Figure 4a) with $L = 6,000$ km, $\Delta x = 100$ km. The standard deviation of the traveltime uncertainty is $\sigma = 0.1$ s. (first column) The structures of the input plume models. (second and third columns) The resolved velocity structures using FF and RT. The dotted line is the 660 discontinuity. (fourth column) The resolved velocity structure along the plume axis for FF (in blue) and RT (in green), as well as the strength of the input structure δV_S^{IN} (in grey). The anomalies below the 660 are enlarged by a factor of 2 relative to the upper mantle for clarity.

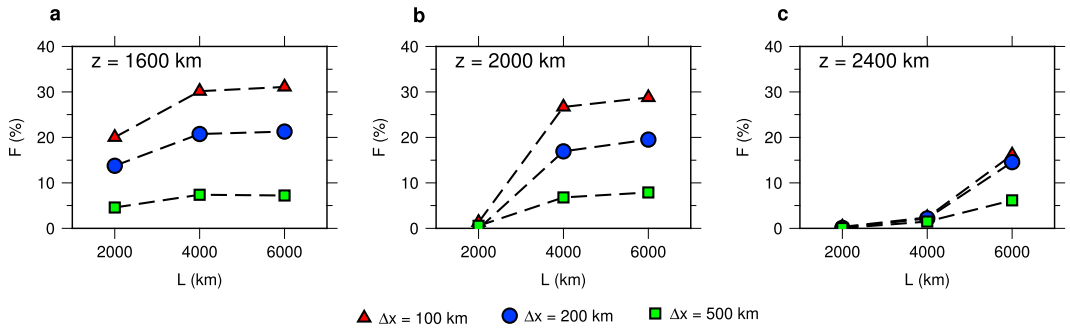

Figure 6. The fraction *F* recovered of the velocity anomaly within the tail of R1b as a function of network width *L*. *F* is determined for a station spacing Δx of 100 km (triangles), 200 km (circles), and 500 km (squares) and for three depths along the plume axis: (a) 1,600 km, (b) 2,000 km, and (c) 2,400 km. Delay times are inverted using FF.

The width of the plume tail is a primary factor in determining the fraction of the input anomaly recovered. Plume R3 has the thinnest tail (less than 400 km wide) and is resolved with the greatest amplitude reduction. With FF the tail is imaged with an amplitude $\delta V_S = -0.5\%$, which is only about 25% of the strength of the input structure. With RT, the shear velocity reduction δV_S in the tail is smaller than 0.1%, which we consider to be undetectable. The tails of plumes R1b and R1c are slightly wider (about 500 km wide) and are recovered with greater amplitude. In the lowermost mantle, with FF, the tails of R1b and R1c are imaged with an amplitude of about $\delta V_S = -1\%$, which is about 30% of the amplitude of the input structure. In the midmantle, R1c is imaged with greater amplitude than R1b since the tail of R1b thins slightly near 1,500 km depth. With RT, the tails of R1b and R1c are close to invisible in the lowermost mantle (δV_S of about −0.2%). The wide plume tail of R2 (diameter of 800 km) is imaged with the highest amplitude. More than 50% of the initial anomaly is recovered to a depth of 1,800 km (imaged amplitude $\delta V_S < -2\%$). Near the base of the mantle the tail diminishes in strength to about $\delta V_S = -1\%$. The broad lower mantle plume head of R1a is imaged with little amplitude reduction with both FF and RT (about 75% of strength of the input structure), but the short stem is less accurately recovered.

4.2. Effects of Network Spacing and Aperture

Image resolution depends on wave path coverage. Networks with dense station spacing offer data redundancy and enable resolution of fine-scale structure. Depth resolution is best for the network with the widest aperture as teleseismic wave crisscross the mantle at large range of angles.

To illustrate how image resolution depends on network aperture and station density, we show in Figure 6 the resolved fractional amplitude *F* with respect to the shear velocity anomaly in the input model: $F = \delta V_S^{\mathrm{OUT}} / \delta V_S^{\mathrm{IN}}$. For plume R1b and using FF, we determine *F* at three depths along the plume axis in the lower mantle. We use network configuration A for values of *L* of 2,000 km, 4,000 km, and 6,000 km and Δx of 100 km, 200 km, and 500 km. The standard deviation of delay time measurement error is $\Delta\sigma = 0.1$ s.

Resolution decreases with increasing depth *z* because data coverage diminishes. For the smallest width ($L = 2,000$ km), teleseismic *S* waves do not cross the plume axis at depths larger than 2,000 km so $F = 0$ regardless of the station spacing Δx. When $L = 4,000$ km, the plume tail is resolved to over 2,000 km depth. There is a weak signal of plume tail at 2,400 km depth only when the network width is $L = 6,000$ km. However, the narrow plume tail is resolved with a significant amplitude reduction. At 1,600 km depth, *F* in the plume tail is lower than 30% for the widest width *L* of 6,000 km and the smallest station spacing Δx of 100 km considered. *F* decreases with increasing station spacing because the data misfit contributes less to the object function *O* (equation (3)).

4.3. *P* velocity Versus *S* Velocity Inversion

Figure 7 shows a comparison between *S* wave and *P* wave inversions for plume R1c using FF theory. We use configuration A and $L = 6,000$ km, and $\Delta x = 100$ km and assume that the standard deviation of random traveltime error $\sigma = 0.1$ s. Throughout the lower mantle, *S* wave inversions recover a larger fraction of the input anomaly than *P* wave inversions. The velocity anomaly in the lower mantle is about −1.0% for *S* (30% of the amplitude in the input structure) and −0.3% for *P* (15% of the amplitude in the input structure).

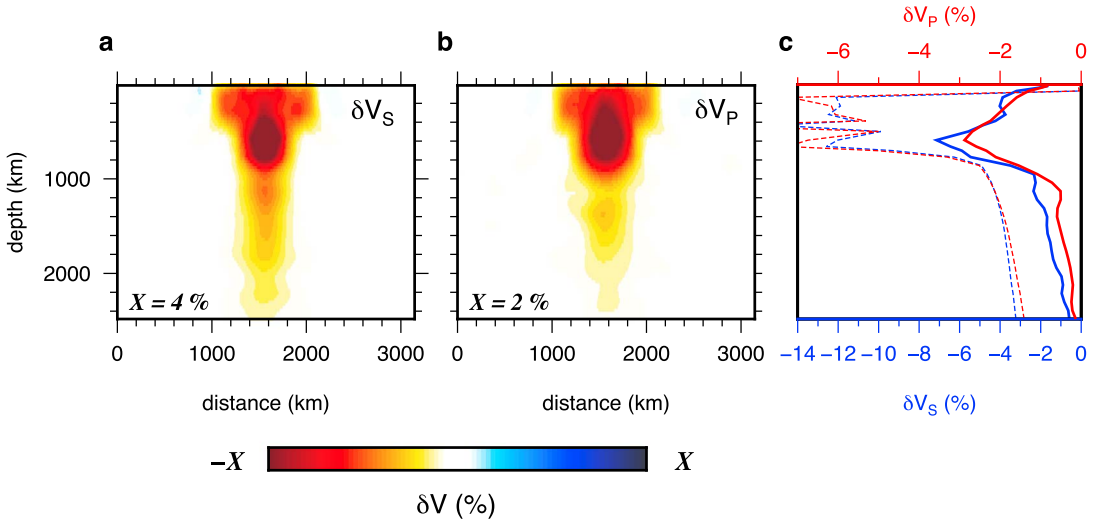

Figure 7. Comparison of (a) the resolved *S* wave velocity δV_S and (b) the resolved *P* wave velocity δV_P structures for plume R1c using the idealized source-receiver geometry and FF theory. The scale *X* of the color bar is indicated in the bottom left corner. (c) shows δV_S (blue) and δV_P (red) along the plume axis. Dashed lines indicate the axial anomaly of the input model.

There are two reasons for the higher amplitudes of *S* velocity anomalies. First, δV_S is stronger than δV_P in the input structures by about a factor of 2 due to the greater sensitivity of V_S to temperature. Second, the *P* wave has a larger wavelength, a wider Fresnel zone, and is more susceptible to the effects of wavefront healing. Given its wider Fresnel zone, a *P* wave is sensitive to structure in the mantle over a broader volume than *S* waves and *P* velocity heterogeneity is imaged with a lower amplitudes. We note that we are comparing inversions of *P* and *S* wave delays calculated in the same frequency band. In practice, *P* waves may be analyzed at higher frequencies than *S* waves. If *P* delays are determined at a period of $T = 5$ s, we expect to recover the same fraction of the plume tail because the sensitivity kernels of *P* and *S* would be of comparable size.

4.4. The Effect of Measurement Uncertainty

To test the effect of uncorrelated error in travel time measurements, we invert *S* wave delay times with variable amounts of assumed noise. We use configuration A with $L = 6,000$ km and $\Delta x = 200$ km and choose three values for the standard deviation of traveltime error: $\sigma = 0.1$ s, $\sigma = 0.5$ s, and $\sigma = 1.0$ s. We test the effects for plume R1b using FF.

With increasing values of σ, model damping and regularization have higher influence (see equation (3)). This is evident from the comparison of the resolved structure of plume R1b for the three values of σ in Figure 8. When the traveltime error is smallest (i.e., $\sigma = 0.1$ s), the deep plume tail is resolved with an amplitude of

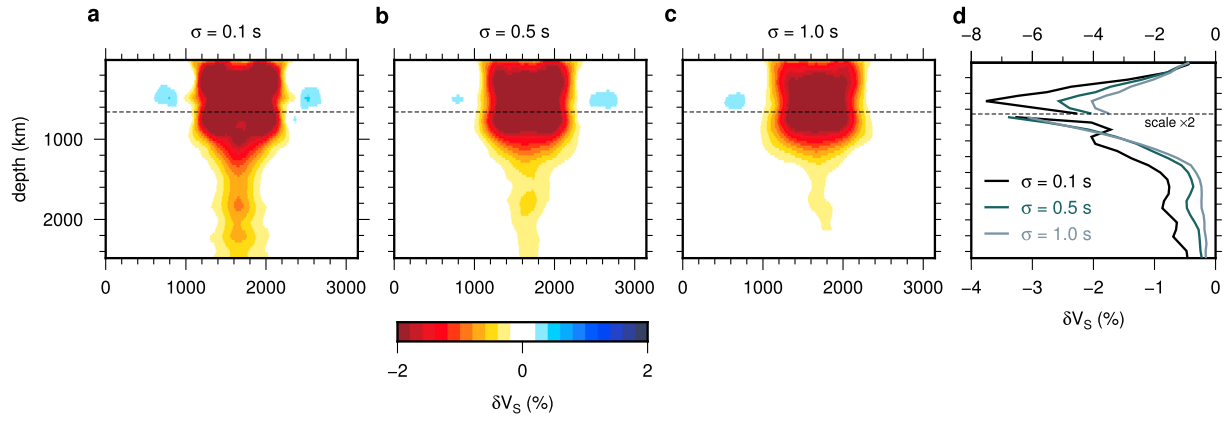

Figure 8. Effect of Gaussian noise in the traveltime measurements on tomographic imaging of plumes using FF and *S* traveltime delays. (a–c) FF *S* wave inversion results of R1b, with different values for the standard deviation of Gaussian noise σ. (d) The structure of each of the three models along the plume axis. The scale of the *x* axis is enlarged by a factor of 2 in the lower mantle.

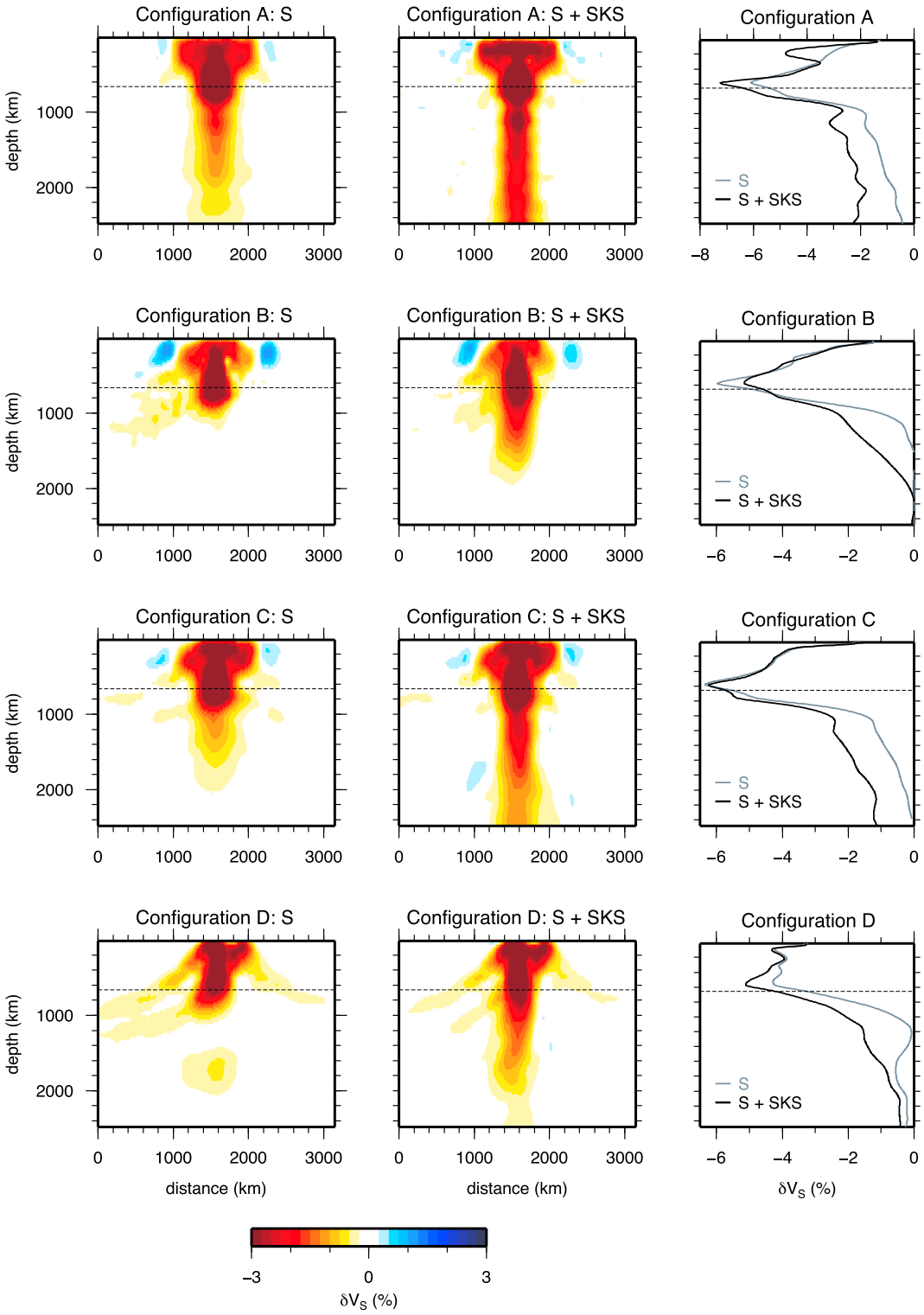

Figure 9. Inversions of R1c for all source-receiver configurations using FF. The rows correspond to (i) the idealized rectangular grid, (ii) the PLUME geometry, (iii) the intersecting linear arrays, and (iv) the Pacific array. (left column) Models use only *S* traveltimes and (middle column) models use *S* and *SKS* traveltimes. (right column) Comparison of inversion results for *S* and *S* + *SKS* along the plume axis.

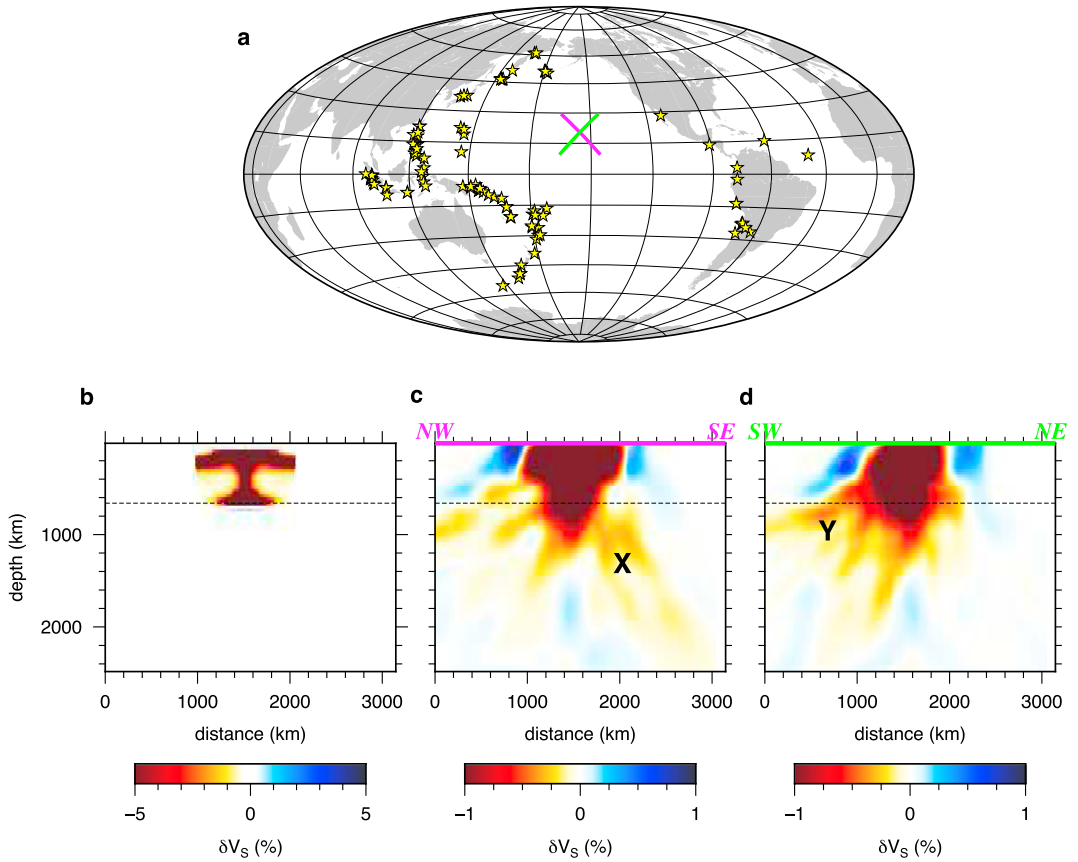

Figure 10. Smearing test for the PLUME experiment (i.e., configuration B). *S* and *SKS* traveltimes are jointly inverted using FF. (a) Earthquake distribution used in the inversion, as well as the locations of cross sections through recovered model. (b) Input plume structure, which is the upper mantle expression of R1c (i.e., R1c where the plume tail has been artificially removed). (c) NW-SE cross section through the recovered model. The feature labeled "X" illustrates smearing oriented steeply to the SE due to the prevailing incoming ray direction of South American events. (d) SW-NE cross section through recovered model. The feature labeled "Y" reflects smearing to the SW owing to the prevalence of South Pacific events.

$\delta V_S \approx -1.0\%$. For $\sigma = 0.5$ s, the recovered shear velocity anomaly in the plume tail is δV_S is weaker than −0.2% and the resolved δV_S is smaller than −0.1% for $\sigma = 1.0$ s. These weak anomalies are likely undetectable.

4.5. Comparison Between Networks

Figure 9 compares the resolved images of plume R1c for the four network configurations discussed in section 4. We assume that $\sigma = 0.1$ s and invert the delay times using FF. We invert either the delay time of *S* (Figure 9, left column) and *S* with *SKS* (Figure 9, middle column).

High data coverage is key for the imaging of the plume tail in the lower mantle. The images obtained using the optimal experiment geometry are shown in Figure 9 (first row) (see also Figure 4). They exhibit signatures of the tail of plume R1c deep into the lower mantle. The shear velocity anomaly δV_S in the plume tail is lower for configuration B (representative of the PLUME network around Hawaii) because the aperture is much smaller and the event distribution is inhomogeneous. When distributing a similar number of stations as in B into wide-aperture linear arrays (configuration C), the imaging of the deep mantle structure is significantly better. The Pacific Array distribution of stations across the Pacific Ocean (configuration D) produces a weak signature of the tail in the lower mantle. However, without dense station coverage the images are missing a clear mantle-wide expression of plume R1c into the upper mantle. We note that resolution in the middle and shallow mantle can be improved by incorporating surface reflections (e.g., seismic phase (SS)) and surface wave constraints.

Figure 9 demonstrates also that *SKS* traveltimes provide resolution of the structure in the lower mantle. For example, for configuration A the shear velocity anomaly δV_S in the plume tail diminishes from about −2.0%

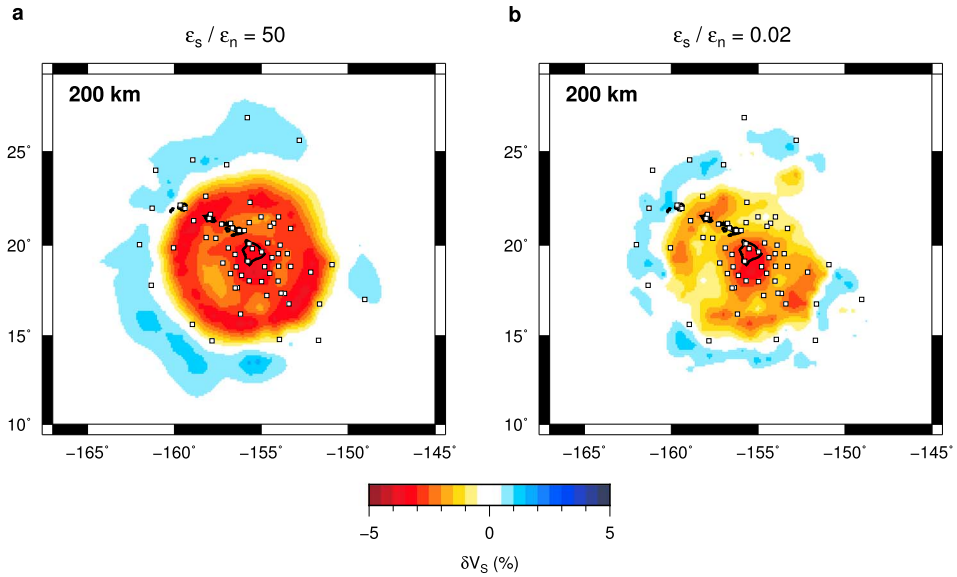

Figure 11. Effect of regularization parameters. Inversions shown are for R1b using *S* and *SKS* travel times, and the PLUME geometry. Horizontal slices of the model are taken at 200 km depth. (a) Smooth models are preferred ($\epsilon_s/\epsilon_n = 50$) and (b) small models are preferred ($\epsilon_s/\epsilon_n = 0.02$).

at 1,000 km depth to less than −1.0% near the base of the mantle when only *S* traveltime delays are inverted. A joint inversion of *S* and *SKS* traveltime delays produces a nearly constant δV_S of −2.0% in the plume tail throughout the lower mantle.

4.6. The Resolving Power of *SKS*

Wolfe et al. (2009) concluded that *SKS* is capable of driving resolution of the deep mantle where direct *S* waves are absent. Our results confirm this, as is evident in Figure 9 (second row), which shows R1c imaged with the PLUME network (i.e., configuration B). When inversions are performed using only *S* (first panel), the plume is not imaged below a depth of 1,000 km. When *SKS* is included (second panel), the plume tail is apparent to a depth of 1,800 km.

However, since *SKS* propagates nearly vertically through the mantle, it is difficult to resolve structure in the upper mantle and lower mantle independently. To illustrate this, plume head in the upper mantle, we compute and invert *S* and *SKS* travel time delays for the same plume R1c in which we have set $\delta V_S = 0$ in the lower mantle (Figure 10a). The NW-SE and SW-NE oriented cross sections in Figures 10b and 10c indicate that upper mantle structure is projected into the lower mantle along dominant *S* and *SKS* paths. For instance, the steeply dipping anomaly in Figure 10c, labeled X, projects toward a cluster of events in South America at large epicentral distances that produces most of the *SKS* traveltime delays. In Figure 10d the more shallowly dipping anomaly Y has a direction toward the SW, parallel to *S* wave paths between Hawaii and Tonga. Similar artifacts toward the NE are missing because only one event in North America contributes to the collection of traveltime delays.

4.7. Fast Anomalies Due To Regularization

When data coverage is sparse, regularization artifacts tend to dominate tomographic images. In particular, when strong preference is given to smooth models, artificial high-to-low seismic velocity oscillations may be introduced. Figure 11 shows inversion results for R1b imaged with configuration B, in which a high-velocity ring-shaped anomaly is introduced surrounding the plume head in the upper mantle. The amplitude of the feature is as large as $\delta V_S = +1.0\%$ and could be misinterpreted as dynamic in origin. The artifact is several hundred kilometers wide in some cases, which is much wider than the blocks used in the model parameterization. A notable gap in the ring anomaly is present NE of Hawaii due to a lack of raypath coverage from North American events. The strength and extent of the artifact depends on the choice of regularization. Figure 11a shows an inversion with $\epsilon_s/\epsilon_n = 50$ (strong preference for smooth models), and Figure 11b shows an inversion with $\epsilon_s/\epsilon_n = 0.02$ (strong preference for small models). In both cases, the fast ring anomaly is present; however, it is more prominent when preference is given to smoothness.

The tradeoff for minimizing the high-velocity artifact (i.e., giving stronger preference to norm damping) is that a smaller fraction of the true strength of the plume is recovered.

5. Discussion

The Hawaii PLUME network has been one of the most comprehensive experiments for studying the structure the mantle beneath a hot spot. It comprised an array of both on-shore and offshore seismic instrumentation designed to maximize imaging resolution given the constraints on budget and operational logistics. We have also focused on the PLUME experiment in our analysis to illustrate how the imaging of a plume tail in the deep mantle beneath a regional seismic network is complicated by the limited array aperture and inhomogeneous data coverage.

Our analysis confirms that the PLUME experiment is capable of imaging deep mantle structure if traveltime measurements of *SKS* are incorporated in the analysis. However, the limited vertical resolution complicates the interpretation of teleseismic traveltime tomography images. Seismic structure in lower mantle cannot be resolved independently from structure in the upper mantle from regional network data. Our simple test (shown in Figure 10) illustrates how seismic structure in the upper mantle can be projected into the lower mantle along dominant *S* and *SKS* paths particularly toward regions with high seismicity. Steeply elongated anomalies in the lower mantle follow *SKS* paths to distant earthquakes in South America, while more shallowly dipping anomalies extend to nearer earthquakes in the western Pacific. These anomalies are reminiscent of the anomalies resolved by Wolfe et al. (2009).

However, we do not dismiss the results from Wolfe et al. (2009). In our experiment using the head structure of plume R1c, the velocity reduction in upper mantle is as high as $\delta V_S = -10\%$, corresponding to a temperature anomaly of $\Delta T = 400$ K, which is likely to be unrealistically high. We predict that the velocity anomalies that are projected from an upper mantle plume expression have rather low amplitude ($\delta V_S = -0.3\%$) which is lower than that recovered in the original PLUME experiment (δV_S of about -0.5% extending into the midmantle). While the pattern of smearing is similar between the original experiment and our synthetic analysis, the higher amplitude found in the PLUME experiment may well indicate that a true lower mantle plume expression was recovered.

Over the course of its deployment the EarthScope USArray covered the entire contiguous United States (about 4,000 km wide) with stations typically spaced less than 100 km apart. Recent tomographic images using data from USArray (e.g., Burdick et al., 2017; Porritt et al., 2014; Schmandt et al., 2012) have been used to test the hypothesis that the Yellowstone hot spot has a deep mantle plume origin. Schmandt and Lin (2014) image a mostly vertical slow velocity anomaly beneath Yellowstone to a depth of about 900 km. Porritt et al. (2014) image a slow wave speed anomaly to at least the base of the transition zone and potentially deeper, although below the transition zone the anomaly is weakened and tilted. Our results shown in Figure 6 suggest that a network comparable to USArray is capable of imaging a plume tail to at least 2,000 km depth.

The uncertain detection of a plume tail extending into the deep mantle beneath Yellowstone could be due to several reasons. First, a plume tail may be absent if Yellowstone volcanism is fed by a shallow source, or if the deep plume source is waning. Second, the plume may be thinner or weaker than those we consider and thus impart smaller travel time delays. Uncertainties of travel time observations due to the influence of heterogeneous crust may also make imaging the deep plume tail challenging. Additionally, plume dynamics may be complicated by interaction with the sinking Farallon slab (e.g., Leonard & Liu, 2016).

The imaging of small-scale structure in the deep mantle can potentially be improved either by using multiple-frequency tomography (e.g., Sigloch et al., 2008), which exploits the frequency dependence of body wave dispersion, or full-waveform inversion (FWI) which uses large portions of the seismic signal at broadband frequencies (e.g., Bozdağ et al., 2016; French & Romanowicz, 2015; Rickers et al., 2013). A major challenge of FWI is in distinguishing low-amplitude diffracted arrivals in the coda of main arrivals from crustal scattering. FWI may be particularly useful in regions such as the Pacific Plate surrounding Hawaii where the crust is relatively simple. While FWI may be an improvement over traveltime tomography, we argue that the lack of data coverage is still the limiting factor in the imaging of plume tails in the deep mantle. Our analysis here shows that large-scale ocean-bottom seismometer (OBS) deployments, while costly, can improve seismic models of the deep mantle and advance the plume debate forward significantly.

6. Conclusions

Traveltime tomography is the most powerful tool to image the structure of the deep mantle, but the resolution of small-scale structures such as plume tails is inherently limited. To quantify resolution of thermal plume ascent from the core-mantle boundary, we have investigated how deep mantle plumes are imaged by teleseismic traveltime tomography using regional networks of seismometers and analytical procedures similar to those commonly applied to real data.

We have explored best case scenarios for network design and data coverage and deployments based on past and proposed experiments. Our computations of plume formation at the core-mantle boundary and plume ascent through the mantle incorporate realistic constraints on thermodynamic and rheological conditions of the mantle and plume buoyancy flux. We use mineral physics constraints to relate the elevated temperature to wave speed reductions in the plume. We predict the traveltime delays from 3-D spectral element method waveform simulations at periods longer than 10 s and invert them using both ray theory and finite frequency theory.

Plume tails are imaged with considerably reduced strengths even under ideal imaging conditions. For wide-aperture, dense networks of stations which have recorded earthquakes at a uniform range of azimuths and epicentral distances, a plume tail in the lower mantle is imaged with an amplitude loss of at least 40%. The strength of the imaged plume tail depends on many factors. We have explored the effects of network aperture, station spacing, data types, delay time measurement uncertainty, regularization, and applied modeling theory.

While it is difficult to directly compare "best fit" models for different experiments, the following observations are robust:

1. For the same frequency band *S* velocity tomography provides higher image resolution than *P* velocity tomography since the *S* wave delays are stronger and *S* wave sensitivity zones are smaller.
2. As it accounts for the finite sensitivity zones of waves, finite frequency inversions provide a clearer and higher-amplitude image of the plume tail than ray theoretical inversions.
3. Measurements of traveltime delays of *SKS* contribute to the imaging of plume tails. This supports the argument by Wolfe et al. (2009) that *SKS* extends tomographic resolving power to deeper depths.
4. The uncertainty in the measured traveltime delay poses a significant limitation on resolution. When the measurement uncertainty is larger than about 1.0 s, it is equal to or it exceeds the expected delay time imparted by plume tail in the deep mantle on the *S* wave (see Figure 8 in Maguire et al., 2016). In this case, plume tails cannot be resolved. Hence, accurate estimates earthquake hypocenter locations and event origin times and understanding the effects of the crust and shallow mantle on traveltimes are critical to resolving plumes.
5. Wide-aperture (4,000–6,000 km) networks with dense station coverage (<100–200 km station spacing) are necessary to image narrow (<500 km wide) thermal plume tails. Large-scale deployments of OBS networks could significantly advance plume imaging.

Imaging artifacts appear when data coverage is heterogeneous and the effects of model regularization are relatively large. Due to the predominantly near-vertical wave propagation of teleseismic body waves below a regional network, seismic velocity anomalies are artificially elongated in the vertical direction. The artificial elongation bears a strong resemblance to the resolved anomalies in the lower mantle in the shear velocity model of Wolfe et al. (2009). Ring-shaped high-velocities anomalies surrounding the low-velocity plume anomaly are primarily an effect of regularization. Such artifacts can be minimized by carefully balancing smoothness and norm damping parameters.

Further modeling work should focus on constraining the effects of compositional variability in plumes on their dynamics and seismic velocity expression, as well as assessing travel time delays caused by thermochemical plumes. Additionally, the seismic expression of plumes in whole mantle convection models should be examined.

Acknowledgments
The Computational Infrastructure for Geodynamics provided the code SPECFEM3D-Globe used to compute waveforms. This work is supported by NSF grants EAR-1246700 and EAR-1565511. Computational resources were made available through XSEDE grant TG-EAR15001. We thank two anonymous reviewers and Associate Editor Sebastien Chevrot for helpful reviews. The geodynamic plume models used in our analysis, as well as tables of calculated travel time delays, are available as supporting information in the online version of this paper.

References

Allen, R. M., Nolet, G., Morgan, W. J., Vogfjórd, K., Bergsson, B. H., Erlendsson, P., … Stefánsson, R. (1999). The thin hot plume beneath Iceland. *Geophysical Journal International*, *137*, 51–63. https://doi.org/10.1046/j.1365-246X.1999.00753.x

Ballmer, M. D., Ito, G., Wolfe, C. J., & Solomon, S. C. (2013). Double layering of a thermochemical plume in the upper mantle beneath Hawaii. *Earth and Planetary Science Letters*, *376*, 155–164. https://doi.org/10.1016/j.epsl. 2013.06.022

Ballmer, M., van Keken, P. E., & Ito, G. (2015). Hotspots, large igneous provinces, and melting anomalies, (2nd ed.). In G. Schubert (Ed.), *Treatise on geophysics* (pp. 393–459). Oxford, England: Elsevier. https://doi.org/10.1016/B978-0-444-53802-4.00133-0

Bonnin, M., Nolet, G., Villaseñor, A., Gallart, J., & Thomas, C. (2014). Multiple-frequency tomography of the upper mantle beneath the African/Iberian collision zone. *Geophysical Journal International*, *198*, 1458–1473. https://doi.org/10.1093/gji/ggu214

Bossmann, A. B., & van Keken, P. E. (2013). Dynamics of plumes in a compressible mantle with phase changes: Implications for phase boundary topography. *Physics of the Earth and Planetary Interiors*, *224*, 21–31. https://doi.org/10.1016/j.pepi.2013.09.002

Bozdağ, E., Peter, D., Lefebvre, M., Komatitsch, D., Tromp, J., & Hill, J. (2016). Global adjoint tomography: First-generation model. *Geophysical Journal International*, *207*(3), 1739–1766. https://doi.org/10.1093/gji/ggw356

Burdick, S., Vernon, F. L., Martynov, V., Eakins, J., Cox, T., Tytell, J., … van der Hilst, R. D. (2017). Model update May 2016: Upper–mantle heterogeneity beneath North America from travel–time tomography with global and USArray data. *Seismological Research Letters*, *88*, 319–325. https://doi.org/10.1785/0220160186

Charléty, J., Voronin, S., Nolet, G., Loris, I., Simons, F. J., Sigloch, K., & Daubechies, I. C. (2013). Global seismic tomography with sparsity constraints: Comparison with smoothing and damping regularization. *Journal of Geophysical Research E: Planets*, *118*, 4887–4899. https://doi.org/10.1002/jgrb.50326

Chevrot, S., Martin, R., & Komatitsch, D. (2012). Optimized discrete wavelet transforms in the cubed sphere with the lifting scheme-implications for global finite-frequency tomography. *Geophysical Journal International*, *191*(3), 1391–1402. https://doi.org/10.1111/j.1365-246X.2012.05686.x

Cobden, L., Goes, S., Cammarano, F., & Connolly, J. A. D. (2008). Thermochemical interpretation of one-dimensional seismic reference models for the upper mantle: Evidence for bias due to heterogeneity. *Geophysical Journal International*, *175*(2), 627–648. https://doi.org/10.1111/j.1365-246X.2008.03903.x

Connolly, J. A. D. (2005). Computation of phase equilibria by linear programming: A tool for geodynamic modeling and its application to subduction zone decarbonation. *Earth and Planetary Science Letters*, *236*, 524–541. https://doi.org/10.1016/j.epsl.2005.04.033

Dahlen, F. A., Hung, S.-H., & Nolet, G. (2000). Fréchet kernels for finite-frequency traveltimes—I. Theory. *Geophysical Journal International*, *141*, 157–174. https://doi.org/10.1046/j.1365-246X.2000.00070.x

Dannberg, J., & Sobolev, S. V. (2015). Low-buoyancy thermochemical plumes resolve controversy of classical mantle plume concept. *Nature Communications*, *6*, 6960. https://doi.org/10.1038/ncomms7960

Dziewonski, A. M., & Anderson, D. L. (1981). Preliminary reference Earth model. *Physics of the Earth and Planetary Interiors*, *25*, 297–356. https://doi.org/10.1016/0031-9201(81)90046-7

French, S. W., & Romanowicz, B. A. (2015). Broad plumes rooted at the base of the Earth's mantle beneath major hotspots. *Nature*, *525*, 95–99. https://doi.org/10.1038/nature14876

Gokhberg, A., & Fichtner, A. (2016). Full-waveform inversion on heterogeneous HPC systems. *Computers and Geosciences*, *89*, 260–268. https://doi.org/10.1016/j.cageo.2015.12.013

Grand, S. P. (1987). Tomographic inversion for shear velocity beneath the North American plate. *Journal of Geophysical Research*, *92*, 14,065–14,090. https://doi.org/198710.1029/JB092iB13p14065

Hung, S.-H., Dahlen, F. A., & Nolet, G. (2001). Wavefront healing: A banana–doughnut perspective. *Geophysical Journal International*, *146*, 289–312.

Hwang, Y. K., Ritsema, J., van Keken, P. E., Goes, S., & Styles, E. E. (2011). Wavefront healing renders deep plumes seismically invisible. *Geophysical Journal International*, *187*, 273–277. https://doi.org/10.1111/j. 1365-246X.2011.05173.x

Kawakatsu, H., Ekström, G., Evans, R., Forsyth, D., Gaherty, J., Kennett, B., … Utada, H. (2016). Pacific array (transportable broadband ocean floor array). In *EGU General Assembly Conference Abstracts*, *18*, pp. 2514.

Komatitsch, D., & Tromp, J. (2002). Spectral-element simulations of global seismic wave propagation—I. Validation. *Geophysical Journal International*, *149*, 390–412. https://doi.org/10.1046/j.1365-246X.2002.01653.x

Laske, G., Collins, J. A., Wolfe, C. J., Solomon, S. C., Detrick, R. S., Orcutt, J. A., … Hauri, E. H. (2009). Probing the Hawaiian hot spot with new broadband ocean bottom instruments. *Eos*, *90*, 362–363. https://doi.org/10.1029/2009EO410002

Leonard, T., & Liu, L. (2016). The role of a mantle plume in the formation of Yellowstone volcanism. *Geophysical Research Letters*, *43*, 1132–1139. https://doi.org/10.1002/2015GL067131

Li, X. H., Kind, R., Priestley, K., Sobolev, S. V., Tilmann, F., Yuan, X., & Weber, M. (2000). Mapping the Hawaiian plume conduit with converted seismic waves. *Nature*, *405*, 938–941. https://doi.org/10.1038/35016054

Lin, S.-C., & van Keken, P. E. (2006). Dynamics of thermochemical plumes: 1. Plume formation and entrainment of a dense layer. *Geochemistry, Geophysics, Geosystems*, *7*, Q02006. https://doi.org/10.1029/2005GC001071

Maguire, R., Ritsema, J., van Keken, P. E., Fichtner, A., & Goes, S. (2016). *P*- and *S*-wave delays caused by thermal plumes. *Geophysical Journal International*, *206*, 1169–1178. https://doi.org/10.1093/gji/ggw187

Mercerat, D. E., & Nolet, G. (2013). On the linearity of cross-correlation delay times in finite-frequency tomography. *Geophysical Journal International*, *192*, 681–687. https://doi.org/10.1093/gji/ggs017

Montelli, R., Nolet, G., Dahlen, F. A., Masters, G., Engdahl, E. R., & Hung, S.-H. (2004). Finite-frequency tomography reveals a variety of plumes in the mantle. *Science*, *303*, 338–343. https://doi.org/10.1126/science.1092485

Nolet, G., & Dahlen, F. A. (2000). Wavefront healing and the evolution of seismic delay times. *Journal of Geophysical Research*, *105*, 19,043–19,504.

Porritt, R. W., Allen, R. M., & Pollitz, F. F. (2014). Seismic imaging east of the Rocky Mountains with USArray. *Earth and Planetary Science Letters*, *402*, 16–25.

Rickers, F., Fichtner, A., & Trampert, J. (2012). Imaging mantle plumes with instantaneous phase measurements of diffracted waves. *Geophysical Journal International*, *190*(1), 650–664. https://doi.org/10.1111/j.1365-246X. 2012.05515.x

Rickers, F., Fichtner, A., & Trampert, J. (2013). The Iceland-Jan Mayen plume system and its impact on mantle dynamics in the North Atlantic region: Evidence from full-waveform inversion. *Earth and Planetary Science Letters*, *367*, 39–51. https://doi.org/10.1016/j.epsl.2013.02.022

Schmandt, B., & Lin, F.-C. (2014). *P* and *S* wave tomography of the mantle beneath the United States. *Geophysical Research Letters*, *41*, 6342–6349. https://doi.org/10.1002/2014GL061231

Schmandt, B., Dueker, K. G., Humphreys, E. D., & Hansen, S. (2012). Hot mantle upwelling across the 660 beneath Yellowstone. *Earth and Planetary Science Letters*, *331-332*, 224–236. https://doi.org/10.1016/j.epsl.2012.03.025

Shen, Y., Solomon, S. C., Bjarnason, I. T., & Wolfe, C. J. (1998). Seismic evidence for a lower-mantle origin of the Iceland mantle plume. *Nature*, *395*, 62–65.

Sigloch, K., McQuarrie, N., & Nolet, G. (2008). Two-stage subduction history under North America inferred from multiple-frequency tomography. *Nature Geoscience*, *1*(7), 458–462. https://doi.org/10.1038/ngeo231

Sleep, N. H. (1990). Hotspots and mantle plumes: Some phenomenology. *Journal of Geophysical Research*, *95*, 6715–6736.

Spakman, W., Stein, S., van der Hilst, R., & Wortel, R. (1989). Resolution experiments for NW Pacific subduction zone tomography. *Geophysical Research Letters*, *16*, 1097–1100.

Stixrude, L., & Lithgow-Bertelloni, C. (2011). Thermodynamics of mantle minerals—II. Phase equilibria. *Geophysical Journal International*, *184*, 1180–1213. https://doi.org/10.1111/j.1365-246X.2010.04890.x

Styles, E. E., Goes, S., van Keken, P. E., Ritsema, J., & Smith, H. E. (2011). Synthetic images of dynamically predicted plumes and comparison with a global tomographic model. *Earth and Planetary Science Letters*, *311*, 351–363. https://doi.org/10.1016/j.epsl.2011.09.012

Trampert, J., & Spetzler, J. (2006). Surface wave tomography: Finite-frequency effects lost in the null space. *Geophysical Journal International*, *164*, 394–400. https://doi.org/10.1111/j.1365-246X.2006.02864.x

Wolfe, C. J., Bjarnason, I. T., VanDecar, J. C., & Solomon, S. C. (1997). Seismic structure of the Iceland mantle plume. *Nature*, *385*, 245–247. https://doi.org/10.1038/385245a0

Wolfe, C. J., Solomon, S. C., Laske, G., Collins, J. A., Detrick, R. S., Orcutt, J. A., … Hauri, E. H. (2009). Mantle shear-wave velocity structure beneath the Hawaiian hot spot. *Science*, *326*, 1388–1390. https://doi.org/10.1126/science.1180165

Workman, R. K., & Hart, S. R. (2005). Major and trace element composition of the depleted MORB mantle (DMM). *Earth and Planetary Science Letters*, *231*, 53–72. https://doi.org/10.1016/j.epsl.2004.12.005

Xue, J., Zhou, Y., & Chen, Y. (2015). Tomographic resolution of plume anomalies in the lowermost mantle. *Geophysical Journal International*, *201*, 979–995. https://doi.org/10.1093/gji/ggv067